 CMES, vol.61, no.2, pp.111-132, 2010

Micromechanics-Based Fiber-Bridging Analysis of Strain-Hardening Cementitious Composite Accounting for Fiber Distribution

B.Y. Lee[1], Y. Lee[2], J.K. Kim[3] and Y.Y. Kim[4]

Abstract: In the present work, a micromechanics-based fiber-bridging constitutive model that quantitatively takes into consideration the distribution of fiber orientation and the number of fibers, is derived and a fiber-bridging analysis program is developed. An image processing technique is applied to evaluate the fiber distribution characteristics of four different types of strain-hardening cementitious composites. Then, the fiber-bridging curves obtained from image analysis are compared with those obtained from the assumption of two- and three-dimensional fiber distributions. The calculated ultimate tensile strains are also compared with experimental results. Test results showed that the tensile behavior of strain-hardening cementitious composites can be more accurately predicted and analyzed using the fiber-bridging curve obtained from image analysis.

Keywords: Fiber-bridging Constitutive Model, Strain-Hardening Cementitious Composite, Image Analysis, Fiber Distribution.

1 Introduction

Engineered Cementitious Composite (ECC) is a strain-hardening cementitious composite (SHCC) that incorporates synthetic fibers and exhibits extremely ductile behavior in uniaxial tension, when compared to normal cement-based composites. This behavior is mainly attributed to bridging of micro-cracks by the reinforcing fibers and the resultant multiple cracking. To achieve pseudo strain-hardening behavior based on multiple cracking, two criteria should be satisfied [Leung (1996); Li and Leung (1992)]. The first is the strength condition; specifically, the peak

[1] University of Michigan, Ann Arbor, U.S.A.
[2] Daejeon University, Daejeon, 300-716, Republic of Korea
[3] Korea Advanced Institute of Science and Technology, Daejeon, 305-701, Republic of Korea
[4] Corresponding Author: Chungnam National University, Daejeon, 305-764, Republic of Korea, Phone: +82-42-821-7004, Fax: +82-42-825-0318, E-mail: yunkim@cnu.ac.kr

bridging stress should be larger than the cracking strength. If this condition is satisfied, an immediate stress drop after initial cracking with bridging fibers being pulled out or ruptured is prevented. Otherwise, multiple cracking will not occur. The second is the energy condition. This criterion is for steady state cracking [Marshall and Cox (1988)]. For multiple cracking behavior, a crack should propagate under constant stress and with constant crack opening in order to achieve a uniform stress distribution of fibers. This condition can be defined by the energy balance between the external work, which is the energy necessary to propagate the matrix crack, and the energy dissipated by the bridging fibers. That is, the external work should be equal to the sum of the matrix fracture energy J_{tip} and the energy dissipated by the bridging fibers. The upper limit for the matrix toughness is the complement energy J_b' in the bridging curve. Therefore, J_b' should be larger than J_{tip} (Figure 1). Based on these two criteria, physical phenomenon of multiple cracking can be explained. If the fibers bridging the crack cannot sustain the load, multiple cracking behavior will not appear due to local failure. On the other hand, if the fibers bridging the crack can sustain the load, the fibers will transfer the load to the matrix through their interface, leading to the formation of another crack. This process repeats until local failure in any given crack occurs due to softening in the fiber-bridging behavior.

The fiber-bridging behavior governs the composite tensile behavior. Therefore, control and accurate prediction of the former is very important to successfully design ECC material properties and tensile properties. Micromechanical parameters that affect the fiber-bridging curve include component properties such as fiber length, diameter, elastic modulus, strength, volume fraction, matrix strength, and elastic modulus as well as interfacial properties such as frictional bond strength, chemical bond strength, and slip hardening effect. In addition to micromechanical parameters, fiber orientations affect the fiber-bridging curve.

For a cementitious composite reinforced with three-dimensionally distributed fibers in a random pattern, the peak bridging stress could be 15 to 20% of the peak value of the cementitous composite reinforced with one-dimensionally aligned fibers [Cox (1952)]. The assumption regarding distribution of fiber orientation is thus of primary importance due to its effect on the number of fibers passing the crack plane, the snubbing effect, and strength reduction. The distribution of fiber orientation is affected by the geometry of the specimen and the rheological properties of the composite. However, most researchers analyzed and predicted the mechanical behavior of composites under the assumption of randomly positioned and oriented fibers in fiber reinforced composites [Böhm, Han, and Eckschlager (2004); Yang, Wang, Yang, and Li (2008); Pahr and Böhm (2008); Pyo and Lee (2009)].

In the present work, the authors describe a micromechanical analysis of strain-

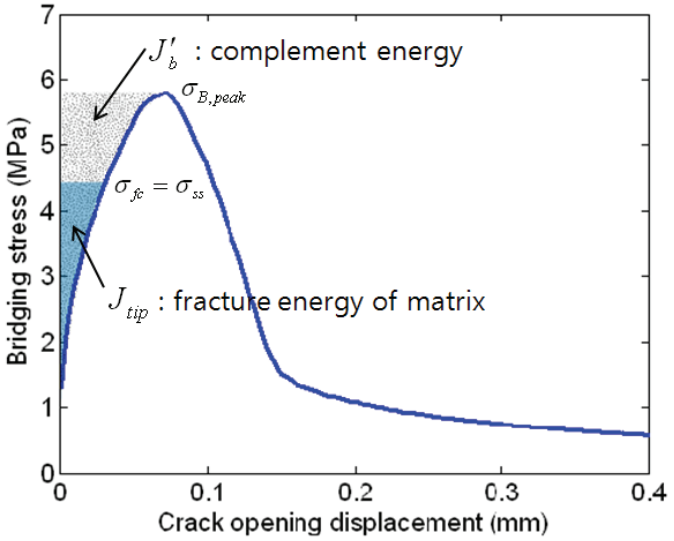

Figure 1: Strength and energy condition for pseudo strain hardening behavior

hardening cementitious composites that accounts for the fiber orientation distribution and the number of fibers. First, the fiber-bridging constitutive law, which quantitatively considers the distribution of fiber orientation and the number of fibers, is derived. In order to evaluate the fiber distribution characteristics, an image processing technique [Lee, Kim, Kim and Kim (2009)] is subsequently applied. The fiber-bridging curves, obtained from an image analysis, are compared with those obtained under the assumption of two-dimensional and three dimensional distributions of the fiber orientation.

2 Fiber-bridging constitutive law

2.1 Modeling of single fiber behavior

Lin et al. [1999] derived a theoretical single fiber debonding and pullout model based on a simple stress analysis and energy balance principle under the following assumptions.

1. The end effect on the total debonding load is negligible. This assumption is generally satisfied for most available fibers (high aspect ratio ($>$100)).

2. The slip-dependent effect is negligible during the debonding stage since relative slippage between the fiber and the matrix in the debonded portion is

small. From this assumption, the frictional stress within the debonded zone remains at a constant τ_0.

3. Poisson's effect is negligible. For flexible fiber/cement systems, Poisson's effect is usually diminished due to inevitable slight misalignment and surface roughness of the fiber.

4. Elastic stretching of the fiber after complete debonding is negligible.

Figure 2 shows the single fiber model. For a given δ , a fiber is debonded or pulled out. In Figure 2, L_e is the embedded length and L is the length of the debonded zone. Lin et al. [1999] derived the relation between P and δ (Eq. (1)) using a force equilibrium condition (Eqs. (2) and (3)) between the fiber and matrix, the compatibility condition, that is, the relation between δ and L (Eq. (4)), and energy conservation for the debonded zone (Eqs. (5) and (6)).

$$P(\delta) = \sqrt{\frac{\pi^2 E_f d_f^3 \tau_0 (1+\eta)}{2}\delta + \frac{\pi^2 E_f d_f^3 G_D (1+\eta)}{2}} \tag{1}$$

where E_f is the elastic modulus of the fibers, d_f is the diameter of the fibers, τ_0 is the frictional stress, and G_D is the chemical bond strength.

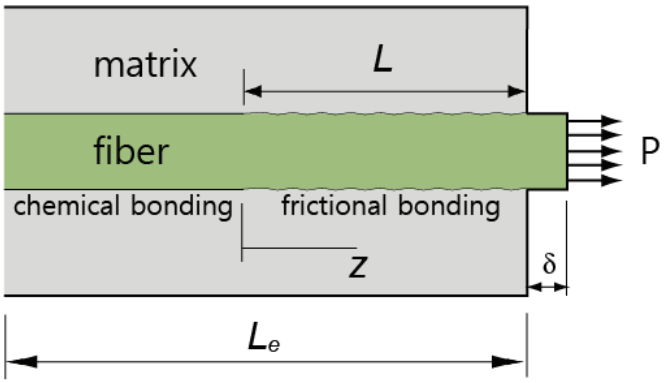

Figure 2: Single fiber model

$$\sigma_f(z) = \sigma_{f0} + \left(z \frac{\sigma - \sigma_{f0}}{L} \right) \tag{2}$$

$$\sigma_m(z) = \sigma_{m0}\left(1 - \frac{z}{L}\right) \tag{3}$$

where σ_{f0} is the normal stress in the fiber, which is obtained by the force equilibrium ($\pi d_f \tau_0 L = (\sigma - \sigma_{f0})\,\pi d_f^2/4$) and σ_{m0} is the normal stress in the matrix, which is obtained by the force equilibrium ($V_f\sigma = V_f\sigma_{f0} + V_m\sigma_m$).

$$\delta = \frac{\sigma L}{E_f} - \frac{2\tau_0 L^2(1+\eta)}{E_f d_f} \tag{4}$$

where $\eta = \frac{V_f E_f}{V_m E_m}$. Eq. (4) is derived from the relative displacement between the fiber and the matrix in the debonded region; that is, $\Delta(z) = u_f(z) - u_m(z)$. This equation can be rewritten as $\frac{d\Delta z}{dz} = \frac{du_f(z)}{dz} - \frac{du_m(z)}{dz} = \frac{\sigma_f(z)}{E_f} - \frac{\sigma_m(z)}{E_m}$, whose boundary condition is $\Delta(z=0) = 0$.

For crack growth dA along the friction surface, energy balance is expressed by the following Eq. (5) [Gao, Mai and Cotterell (1988)].

$$Pdu_f = dU + dW_f + G_D dA \tag{5}$$

where u_f is the displacement, P is the applied load, dU is the change of strain energy, dW_f is the dissipated energy by friction, $G_D dA$ is the fracture energy for chemical bonding.

$$dU = 0.5(Pdu_f - dW_f) \tag{6}$$

This equation gives the energy conservation for the debonded zone, which is assumed to be an elastic system. Based on Eq. (5) and (6), Eq. (7) and (8) can be obtained as follows.

$$\sigma(L) = \frac{4\tau_0 L 1+\eta)}{d_f} + \sqrt{\frac{8G_D E_f(1+\eta)}{d_f}} \tag{7}$$

$$P(L) = \pi d_f \tau_0 (1+\eta) L + \sqrt{\frac{\pi^2 E_f d_f^3 G_D (1+\eta)}{2}} \tag{8}$$

Eq. (4) can be rewritten as Eq. (9) using Eq. (7).

$$\delta = \frac{2\tau_0 L^2(1+\eta)}{E_f d_f} + \sqrt{\frac{8G_D L^2(1+\eta)}{E_f d_f}} \tag{9}$$

If $L = L_e$, the fiber pullout distance (δ_0) for full debonding can be obtained using Eq. (9). After fiber full debonding, the relation between P and δ is given by Eq.

(10), since only frictional bonding stress remains, without chemical bonding stress (Figure 3).

$$P(\delta) = \pi d_f \tau_0 \left[1 + \frac{\delta - \delta_0}{d_f}\beta\right][L_e - (\delta - \delta_0)] \tag{10}$$

where β is the slip-hardening coefficient.

In the above formulation, the crack opening δ is equal to $2u$ during debonding, since debonding occurs on both segments of the crack plane; during frictional pull-out it is equal to u during frictional pull-out, since pull-out occurs on one side segment of the crack plane. Therefore, Eq. (1) and Eq. (9) should be modified as Eq. (11) and Eq. (12), respectively.

$$P(\delta) = \sqrt{\frac{\pi^2 E_f d_f^3 \tau_0 (1+\eta)}{4}\delta + \frac{\pi^2 E_f d_f^3 G_D (1+\eta)}{2}} \tag{11}$$

$$\delta_0 = \frac{4\tau_0 L_e^2 (1+\eta)}{E_f d_f} + 4\sqrt{\frac{2G_D L_e^2 (1+\eta)}{E_f d_f}} \tag{12}$$

The effect of the fiber orientation, known as the "snubbing effect", in the relation between P and δ is expressed as Eq. (13) [Morton and Groves (1976); Li (1992)].

$$P(\theta) = P(0)\, e^{f\theta} \tag{13}$$

The effect of fiber orientation in the relation between fiber strength σ_{fu} and δ is expressed as Eq. (14) [Lin, Kanda and Li (1999)].

$$\sigma_{fu}(\theta) = \sigma_{fu}(0)\, e^{-f'\theta} \tag{14}$$

where f and f' are the snubbing effect coefficient and fiber strength reduction coefficient and are determined by curve-fitting experimental data. Wu [2001] measured f using Polyvinyl Alcohol (PVA) fiber having 0.5% oiling coating and found that f ranged from 0.2 to 0.8. Kanda et al. [Kanda and Li (1998)] found that f' was approximately 0.3 for the fiber/matrix system they investigated.

2.2 Modeling of multiple fibers behavior accounting for fiber distribution

For one dimension, the fiber number in a unit area is expressed by Eq. (15)

$$N_{1D} = \frac{V_f}{A_f} \tag{15}$$

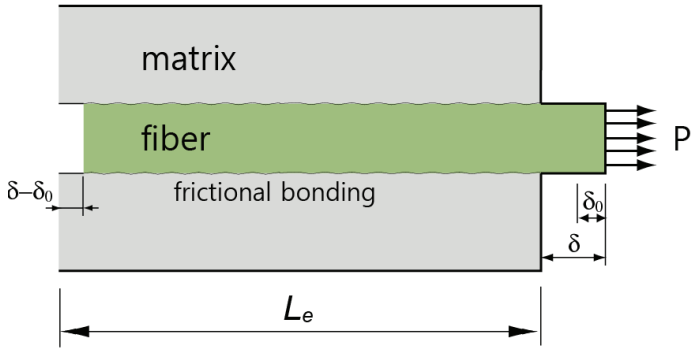

Figure 3: Single fiber model after full debonding

where V_f and A_f are the volume and the area of fiber, respectively. Figure 4 shows the embedded length with the inclination angle. In Figure 5, z is the centroidal distance. If $p(\theta)$ and $p(z)$ are probability density functions for θ and z, the number of fibers in a unit area is expressed as Eq. (16).

$$N_B = N_{1D} \int_{\theta_1}^{\theta_2} \int_{z_1}^{z_2} p(z) dz p(\theta) d\theta \tag{16}$$

For three dimensions, $p(z)$ is $2/L_f$ and $p(\theta)$ is $\sin(\theta)$. If θ_1 is 0 and θ_2 is $\pi/2$, z_1 should be 0 and z_2 $(L_f/2)\cos\theta$, since L_e (Eq. (17)) should not be less than 0.

$$L_e = \frac{L_f}{2} - \frac{z}{\cos\theta} \tag{17}$$

By changing the variable z to L_e, Eq. (16) can be rewritten as Eq. (18).

$$N_B = N_{1D} \int_0^{\pi/2} \int_0^1 p(L_e)\, p(\theta) \cos(\theta) dL_e d\theta \tag{18}$$

If the resistance force of a single fiber at the crack plane is $P(\theta, L_e, \delta)$, the composite bridging property can be expressed as Eq. (19).

$$\sigma_B(\delta) = \frac{4V_f}{\pi d_f^2} \int_0^{\pi/2} \int_0^{L_f/2} P(\theta, L_e, \delta) p(\theta) \cos(\theta)\, dL_e d\theta \tag{19}$$

If N_m is the number of fibers measured using the image processing technique and A_m is the measured area, Eq. (19) should be changed to the following equation.

$$\sigma_B(\delta) = \alpha_{nf} \frac{4V_f}{\pi d_f^2} \int_0^{\pi/2} \int_0^{L_f/2} P(\theta, L_e, \delta) p(\theta) cos(\theta)\, dL_e d\theta \tag{20}$$

where α_{nf} is the fiber number coefficient, which means the ratio of measured fiber numbers and assumed fiber numbers and can be expressed by Eq. (21).

$$\alpha_{nf} = \frac{\pi d_f^2 N_m}{4V_f A_m \int_0^{\pi/2} \int_0^{L_f/2} p(\theta)\cos(\theta)\, dL_e d\theta} \tag{21}$$

where N_m is the number of fiber measured using image processing technique and A_m is the measured area. Eq. (21) is derived by $\alpha_{nf}\frac{4V_f}{\pi d_f^2}\int_0^{\pi/2}\int_0^{L_f/2} p(\theta)\cos(\theta)\, dL_e d\theta = \frac{N_m}{A_m}$.

On the basis of Eqs. (10) – (14), (20), and (21), the composite bridging property can be expressed as Eq. (22).

$$\begin{aligned}
\sigma_B(\delta) &= \alpha_{nf}\frac{4V_f}{\pi d_f^2} \\
&\int_{\theta_1}^{\theta_2}\int_{L_{e1}}^{L_{e2}} \sqrt{\frac{\pi^2 E_f d_f^3 \tau_0 (1+\eta)}{4}\delta + \frac{\pi^2 E_f d_f^3 G_D (1+\eta)}{2}} e^{f\theta} p(\theta)\cos(\theta) d\theta dL_e \\
&+ \alpha_{nf}\frac{4V_f}{\pi d_f^2} \\
&\quad \int_{\theta_3}^{\theta_4}\int_{L_{e3}}^{L_{e4}} \pi d_f \tau_0 \left[1 + \frac{(\delta-\delta_0)}{d_f}\beta\right][L_e - (\delta-\delta_0)]\delta e^{f\theta} p(\theta)\cos(\theta)\, d\theta dL_e
\end{aligned} \tag{22}$$

where $L_{e1}, L_{e2}, L_{e3}, L_{e4}, \theta_1, \theta_2, \theta_3$,and θ_4 are determined according to δ.

Eq. (22) can be rewritten using the normalized length divided by $L_f/2$, as expressed in Eq. (23).

$$\begin{aligned}
\sigma_B\left(\overline{\delta}\right) &= \alpha_{nf}\frac{4V_f}{\pi d_f^2} \\
&\int_{\theta_1}^{\theta_2}\int_{\overline{L}_{e1}}^{\overline{L}_{e2}} \sqrt{\frac{\pi^2 E_f d_f^3 \tau_0 (1+\eta)}{4}\overline{\delta}\frac{L_f}{2} + \frac{\pi^2 E_f d_f^3 G_D (1+\eta)}{2}} e^{f\theta} p(\theta) cos(\theta)\, d\theta d\overline{L}_e \\
&+ \alpha_{nf}\frac{4V_f}{\pi d_f^2} \\
&\quad \int_{\theta_3}^{\theta_4}\int_{\overline{L}_{e3}}^{\overline{L}_{e4}} \pi d_f \tau_0 \left[1 + \frac{\overline{\delta}-\overline{\delta}_0}{d_f}\frac{L_f}{2}\beta\right]\left[\overline{L}_e - (\overline{\delta}-\overline{\delta}_0)\right]\frac{L_f}{2} e^{f\theta} p(\theta) cos(\theta)\, d\theta d\overline{L}_e
\end{aligned} \tag{23}$$

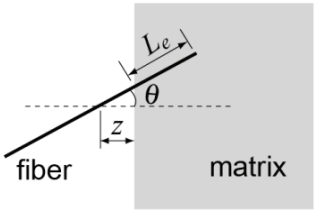

Figure 4: Embedded length with inclination angle

2.3 Effect of matrix spalling

Matrix spalling is observed in a brittle and low strength matrix. Typical results in the embedded strength tests show that the fibers rupture for different inclining angles θ and they tend to rupture at lower stress as θ increases. This load drop is attributed to matrix spalling, as evidenced by microscopy observations [Kanda and Li (1998)].

An inclined fiber exerts additional force and stress concentration on the matrix, i.e., the reaction force of the pulley at the supporting point. If the stress induced on matrix at the supporting point is greater than the strength of matrix, the matrix will be spalled. The size of the spalled matrix section is governed by the external load on the fiber, the matrix strength, the matrix stiffness, and the fiber orientation. A semi-empirical equation for estimating the spalling size s is proposed (Eq. (24)) as follows [Yang, Wang, Yang and Li (2008)].

$$s = \frac{P\sin\left(\frac{\theta}{2}\right)}{kd_f\sigma_{mu}\cos^2\left(\frac{\theta}{2}\right)} \tag{24}$$

where P is the external force acting on the fiber, θ is the orientation of the fiber, σ_{mu} is the matrix tensile strength, and k is the spalling coefficient. k is constant in relation to the fiber geometry and matrix stiffness.

Figure 5 schematically illustrates inclined bridging with matrix spalling. Matrix spalling changes the fiber orientation θ to a smaller θ' and decreases the embedded length (L_e) by $2s$. This may cause a load drop as well as delay the fiber rupture under displacement control. δ' and θ' can be expressed as Eq. (25) and Eq. (26), respectively.

$$\delta' = \sqrt{4s^2 + 4s\delta\cos\theta + \delta^2} \tag{25}$$

$$\theta' = \sin^{-1}\left(\frac{\delta\sin\theta}{\delta'}\right) \tag{26}$$

To depict the load drop according to the change of embedment length and orientation caused by matrix spalling, Eq. (8) is changed to Eq. (27) in the case of debonding fibers.

$$P(L) = \pi d_f \tau_0 (1+\eta)(L-s) + \sqrt{\frac{\pi^2 E_f d_f^3 G_D (1+\eta)}{2}} \tag{27}$$

where L can be obtained from Eq. (28), which is derived from Eq. (12).

$$L = \frac{\sqrt{E_f d_f}}{2\tau_0 (1+\eta)} \left[\sqrt{2(1+\eta)(G_D + \tau_0 \frac{\delta}{2})} - \sqrt{2(1+\eta) G_D} \right] \tag{28}$$

For pulling out fibers, Eq. (10) is changed to Eq. (29)

$$P(\delta) = \pi d_f \tau_0 \left[1 + \frac{\delta - \delta_0}{d_f} \beta \right] [L_e - s - (\delta - \delta_0)] \tag{29}$$

Therefore, this load leads to the stress on the fiber, which is expressed as Eq. (30) considering the snubbing effect.

$$\sigma_f = \frac{4P}{\pi d_f^2} e^{f\theta'} \tag{30}$$

A fiber will be ruptured when the following equation is satisfied.

$$\sigma_f \geq \sigma_{fu}(0)\, e^{-f'\theta'} \tag{31}$$

Eq. (23) can be rewritten as Eq. (32) using Eqs. (27) – (29).

$$\begin{aligned}
&\sigma_B\left(\overline{\delta}\right) = \alpha_{nf} \frac{4V_f}{\pi d_f^2} \\
&\int_{\theta_1}^{\theta_2} \int_{\overline{L}_{e1}}^{\overline{L}_{e2}} \pi d_f \tau_0 (1+\eta)(\overline{L} - \overline{s}) \frac{L_f}{2} \sqrt{\frac{\pi^2 E_f d_f^3 G_D (1+\eta)}{2}} e^{f\theta'} p(\theta) cos(\theta)\, d\theta d\overline{L}_e \\
&+ \alpha_{nf} \frac{4V_f}{\pi d_f^2} \\
&\int_{\theta_3}^{\theta_4} \int_{\overline{L}_{e3}}^{\overline{L}_{e4}} \pi d_f \tau_0 \left[1 + \frac{\overline{\delta} - \overline{\delta}_0}{d_f} \frac{L_f}{2} \beta \right] \left[\overline{L}_e - \overline{s} - (\overline{\delta} - \overline{\delta}_0) \right] \frac{L_f}{2} e^{f\theta'} p(\theta) cos(\theta)\, d\theta d\overline{L}_e
\end{aligned} \tag{32}$$

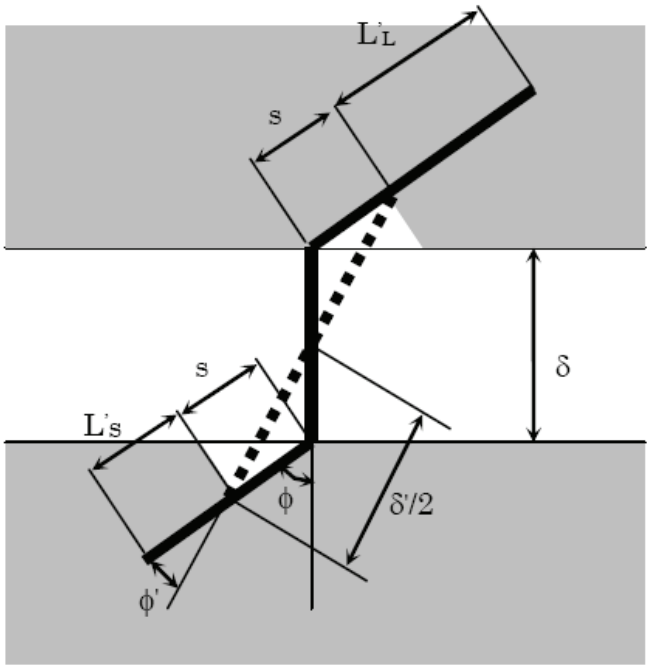

Figure 5: Schematic diagram of inclined bridging with matrix spalling [Yang, Wang, Yang and Li (2008)]

If the distribution of the fiber orientation is measured from an image analysis, $p(\theta)$ is replaced by the following function proposed by Xia et al. [1995].

$$g(\theta) = \frac{(sin\theta)^{2p-1}(cos\theta)^{2q-1}}{\int_{\theta_{min}}^{\theta_{max}}(sin\theta)^{2p-1}(cos\theta)^{2q-1}d\theta} \tag{33}$$

where p and q are the shape parameters, which can be used to determine the shape of the probability density function. The parameters p and q should be more than 1/2. θ falls in a range from 0 to π /2.

Figure 6 shows the numerical procedure for calculation of the bridging curve. For given micromechanical parameters and assumed crack opening, the stress of each fiber according to L_e and θ is calculated. If the stress of the fiber is greater than the fiber strength considering the fiber strength reduction caused by fiber inclination, the stress of the fiber will be zero due to rupture. The bridging stress is then calculated by numerical integration. This process is repeated with increased crack opening until the assumed crack opening is larger than the final crack opening, that

is, $L_f/2$.

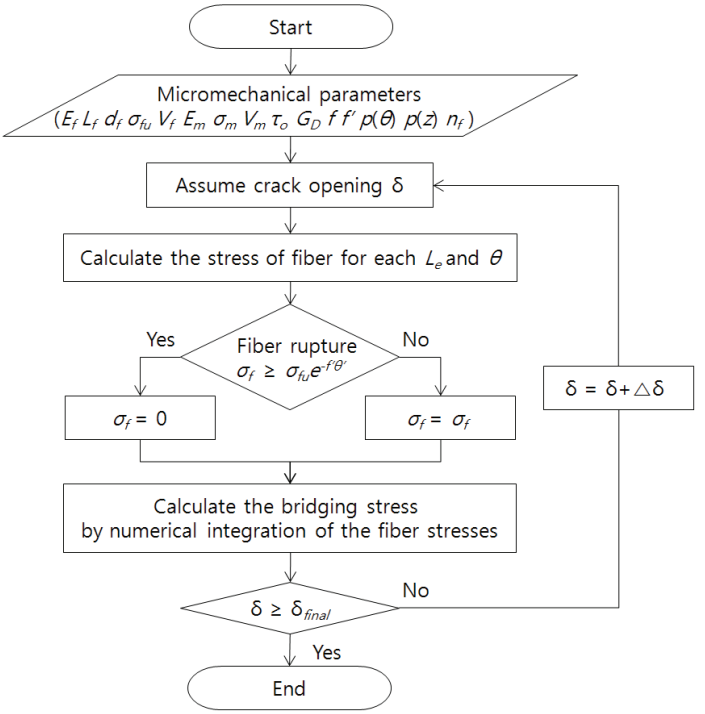

Figure 6: Numerical procedure for calculation of fiber bridging curve

3 Fiber distribution evaluation

Lee et al. [2009] proposed an enhanced evaluation technique of PVA fiber dispersion in cementitious composites. The proposed evaluation technique is composed of stepwise tasks. First, the fiber images detected by a prototype thresholding algorithm are classified into five types by a watershed segmentation algorithm [Vincent and Soille (1991)] and an artificial neural network. Next, aggregate fiber images, that is, misdetected fiber images, are detected correctly by means of the watershed segmentation algorithm and morphological reconstruction [Vincent (1993)]. Figure 7 shows a flow chart of the enhanced detection algorithm. The orientation of the fiber at the cutting plane can be quantitatively calculated by measuring the major axis and minor axis lengths of an ellipse, as expressed by Eq. (34).

$$\theta = \cos^{-1}\left(\frac{l_s}{l_l}\right) \tag{34}$$

where l_s is the minor axis length and is equal to the diameter of the fiber and l_l is the major axis length of the fiber (Figure 8). Table 1 shows artificial fiber images and test results to evaluate the calculation of fiber orientation. The test results demonstrate the accuracy of the calculations, showing relative error within 1%, except for the fiber images with 0° orientation. Relative errors are increased with a decrease of the orientation angle. This is mainly due to the increase of sensitivity with a decrease of the orientation angle in the transformation of the l_s/l_l value into the orientation angle.

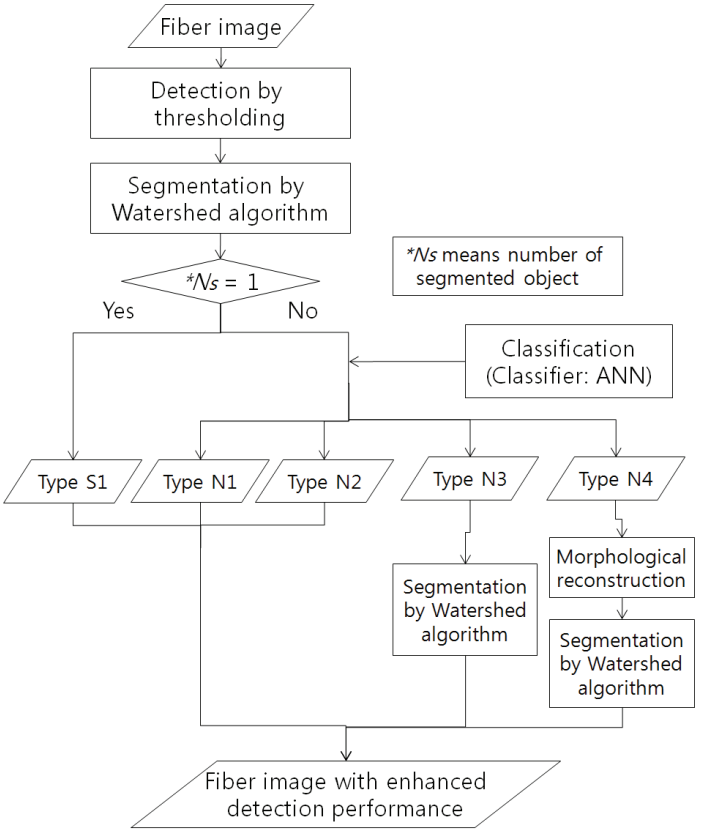

Figure 7: Flow chart of enhanced detection algorithm [Lee et al. (2009)]

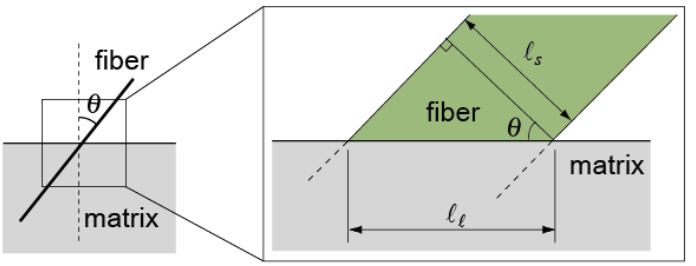

Figure 8: Schematic diagram of an inclined fiber

Table 1: Artificial fiber images and test results to evaluate fiber orientation

Artificial fiber images	Orientation (º)	Calculated orientation (º)	Error (%)
	0	3.62	3.62[a]
	30	29.8	0.719[b]
	45	44.8	0.355[b]
	75	74.9	0.178[b]
	85	84.9	0.0589[b]

[a] Absolute error

[b] Relative error (%)

4 Experimental verification

4.1 Mix proportions and micromechanics parameters

To evaluate the validity of the proposed fiber-bridging constitutive law for strain-hardening cementitious composites, four different types of PVA-ECC were used. The mix proportions and micromechanics parameters of PVA-ECCs are given in Table 2 and Table 3 [Kim et al. (2007)]. A PVA fiber (Kuraray Co. Ltd., REC 15, Japan) was used as the reinforcing fiber with 2% volume fraction. Most micromechanics parameters regarding the matrix were obtained from various tests. The interfacial properties (τ_0, G_D, β) are also obtained from single fiber pullout tests. k, f, and f' are assumed from values reported in the literature (Table 3).

Table 2: Mix proportions

Test variables	Cement	Water	Sand	Slag	HRW[a]	HPMC[b]	V_f (%)
wc60wos	1.0	0.60	0.8	0	0	0.001	2
wc60ws	1.0	0.60	0.8	0.25	0	0.001	
wc48wos	1.0	0.48	0.8	0	0.02	0	
wc48ws	1.0	0.48	0.8	0.25	0.02	0	

[a] High-range water-reducing admixture
[b] Hydroxypropylmethyl-cellulose
All numbers are mass ratios of cement weight except fiber content (volume fraction)

Table 3: Micromechanics parameters

	Micromechanics parameters	wc60wos	wc60ws	wc48wos	wc48ws
Fiber	Fiber length L_f (mm)	12			
	Fiber diameter d_f (mm)	0.040			
	Fiber elastic modulus E_f (GPa)	40			
	Nominal fiber strength σ_{fu}^n (MPa)	1600			
	Apparent fiber strength σ_{fu} (MPa)	1092			
	Fiber volume fraction V_f (%)	2			
	Elongation (%)	6.0			
	Oiling Agent Content (%)	0.8			
Matrix	Elastic modulus E_m (GPa)	17.2	18.4	21.6	26.2
	Splitting tensile strength σ_{sp} (MPa)	3.07	3.54	4.24	4.70
	Spalling coefficient k	500[a]			
Interface	Frictional bond strength τ_0 (MPa)	1.62	1.65	1.82	1.85
	Chemical bond strength G_D (J/m2)	1.82	1.88	1.85	1.83
	Slip-hardening coefficient β	0.0582	0.104	-0.054	0.129
	Snubbing coefficient f	0.30[b]			
	Fiber strength reduction factor f'	0.3[c]			

[a] Assumed on the basis of the referenced paper [Yang et al. (2008)]
[b] Assumed on the basis of the referenced paper [Wu (2001)]
[c] Assumed on the basis of the referenced paper [Kand and Li (1998)]

4.2 Analysis of fiber distribution

Table 4 presents the fiber distribution characteristics and parameters for the distribution function of the fiber orientation. Although the fiber dispersion coefficients show little variation among specimens, ECC specimens with slag have higher values. This means that ECC with slag has more homogeneously distributed fibers in the composites. When the fibers are more homogeneously distributed, the fiber-

bridging capacity may be larger, finally leading to a larger tensile strain capacity. On the other hand, there is no correlation between F_n values and the existence of slag particles. F_n measured by an image analysis may show a smaller value than that calculated by Eq. (18). In this study, there is also no correlation between α_{nf} values and the existence of slag particles. Figure 9 shows the probability density function for the fiber orientation according to the specimens. As can be seen in the figure, the probability density functions measured by the an image analysis are considerably different from those obtained by assuming two- or three-dimensional random distributions for the fiber orientation. That is, the percentage of fibers with smaller angle, which increase the load bearing capacity, between the fiber direction and section direction is larger in the specimens used in this study.

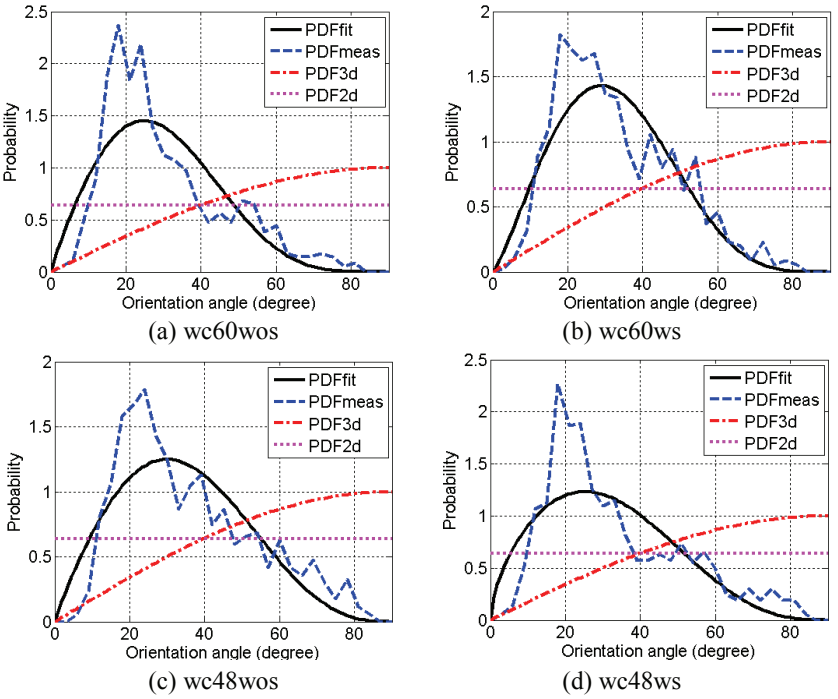

Figure 9: Probability density functions according to mix proportions

Table 4: Fiber distribution characteristics and parameters for distribution function of fiber orientation

	PDF	wc60wos	wc60ws	wc48wos	wc48ws
α_f		0.311(0.0118)	0.321(0.00836)	0.315(0.00550)	0.317(0.000106)
F_n (number/mm^2)	Measured	8.95 (0.391)	9.94 (0.291)	10.6 (0.968)	9.91 (0.144)
	1D	16.7			
	2D	10.7			
	3D	8.37			
Fiber number coefficient (α_{nf})		0.708(0.0599)	0.729 (0.0470)	0.788 (0.0764)	0.789 (0.0415)
p	Measured	0.988(0.0750)	1.03 (0.0866)	0.838 (0.0750)	0.875 (0.0866)
	1D	0.5			
	2D	0.5			
	3D	1			
q	Measured	2.26 (0.605)	2.41 (0.708)	1.74 (0.256)	1.40 (0.367)
	1D	∞			
	2D	0.5			
	3D	0.5			

All data are average values of four specimens and the numerical values in parentheses present the standard deviation

4.3 Fiber-bridging curve according to the distribution of fiber orientation and number of fibers

Fiber-bridging curves according to specimens with different mix proportions considering the distribution of fiber orientation and number of fibers are shown in Figure 10. Fiber-bridging curves predicted on the basis of probability density functions measured using an image analysis are similar with those predicted on the basis of probability density functions assuming a two-dimensional random distribution of fiber orientation. Crack openings corresponding to the peak bridging stress of the bridging curves predicted using an image analysis are larger than those predicted on the basis of the probability density functions assuming a two-dimensional random distribution of the fiber orientation. These differences in crack openings at the peak bridging stress will cause variation in the prediction of the UTS (Ultimate Tensile Strain) capacity of the tensile behavior. Kanda and Li [Kanda and Li (2006)] proposed the stress performance indexes and investigated the effect of those on the UTS. Their results show that the UTS increases with the increase of stress performance index. Table 5 presents the performance indexes according to the fiber distribution and the UTS calculated by using the relation between the stress performance index and the UTS [Kand and Li (2006)]. Figure 11 shows the experimental results of uniaxial tension test performed by Kim et al. [Kim et al. (2007)]. Comparing the UTS calculated on the basis of an image analysis, the relative error between the measured UTS and the calculated UTS is about 15% except the wc48ws specimen. On the other hand, the minimum error between the measured UTS and the UTS calculated on the basis of fiber-bridging curves obtained by assuming two- or three-dimensional random distributions for the fiber orientation exhibit more than 50%. The tensile stress-strain relation of random short-fiber-reinforced cement composites showing pseudo-strain-hardening can be predicted using the first cracking strength, peak bridging stress, and peak crack openings at the peak bridging stress of fiber-bridging curves [Kanda, Lin and Li (2000)]. Therefore, fiber-bridging curves that take into consideration the distribution of fiber orientation and number of fibers as determined via an image analysis are expected to be useful in predicting precisely the tensile stress-strain relation of fiber-reinforced cement composites showing pseudo-strain hardening.

5 Conclusions

A modified fiber-bridging constitutive law that quantitatively considers the distribution of fiber orientation and the number of fibers was derived, and a fiber distribution analysis was conducted on the PVA-ECC specimens with different mix proportions. An image analysis was then performed to obtain fiber-bridging curves

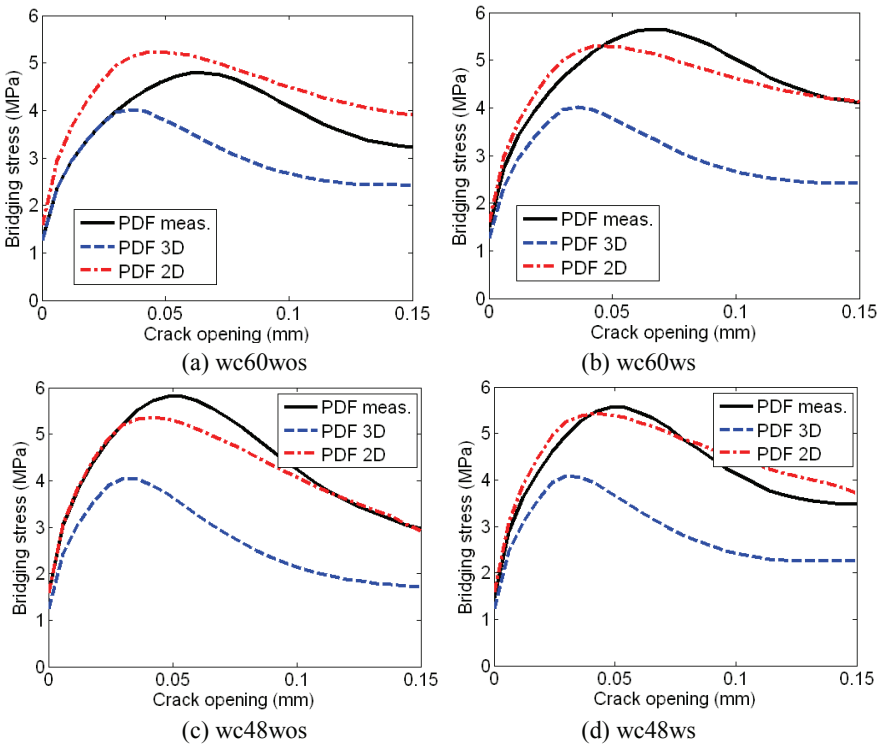

Figure 10: Bridging curve according to the distribution of fiber orientation and number of fibers

from the fiber distribution. These curves were compared with those obtained under the assumption of two-dimensional and three-dimensional distributions of the fiber orientation. Through derivation and verification of the derived fiber-bridging constitutive law, the following conclusions can be drawn from the current results: (1) Probability density functions measured by an image analysis and number of fibers are considerably different from those obtained by assuming two- or three-dimensional random distributions of the fiber orientation. This means that the distribution of fibers is dependent on the flow direction, owing to the casting sequence or shape of the structure. Therefore, it is necessary to evaluate the fiber distribution characteristics; (2) Fiber-bridging curves predicted on the basis of probability density functions measured using an image analysis are similar with those predicted on the basis of probability density functions assuming two-dimensional random distributions of the fiber orientation. However, crack openings at the peak bridging

Table 5: Stress performance index and ultimate tensile strain according to the distribution of fiber orientation

	PDF	wc60wos	wc60ws	wc48wos	wc48ws
Stress performance index	Measured	1.39	1.43	1.25	1.08
	2D	1.53	1.35	1.14	1.04
	3D	1.17	1.02	0.861	0.777
Ultimate tensile strain (%)	Measured	2.77	4.24	0.657	< 0.2
	2D	> 5.0	1.85	0.254	< 0.2
	3D	0.282	< 0.2	< 0.2	< 0.2
Relative error (%)a	Measured	10.8	11.6	17.9	>77.8
	2D	>100	51.3	68.3	>77.8
	3D	88.7	>94.7	>75.0	>77.8

[a] The relative error is calculated as $\left|\mathrm{UTS_{calc}} - \mathrm{UTS_{exp}}\right| / \mathrm{UTS_{exp}} \times 100$

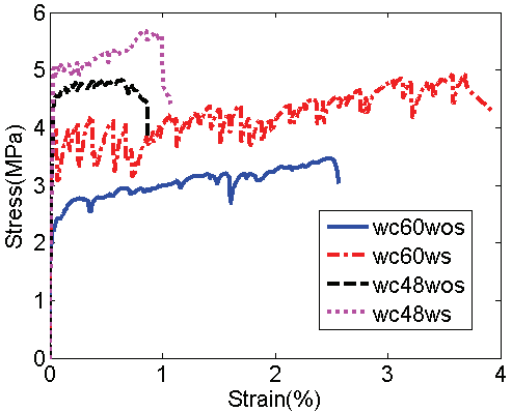

Figure 11: Experimental results of uniaxial tension test [Kim et al. (2007)]

stress of the bridging curves predicted using the an image analysis are larger than those predicted on the basis of the probability density functions assuming a two-dimensional random distribution of the fiber orientation; (3) Comparison results between the calculated UTS and the measured UTS exhibited about 15% error. On the other hand, the minimum error with the UTS calculated from fiber-bridging curves obtained by assuming two- or three-dimensional random distributions for the fiber orientation exhibit more than 50%. Therefore, the tensile behavior of ECC can be precisely predicted and analyzed using the fiber-bridging curve obtained on the basis of the fiber distribution measured using an image analysis.

Acknowledgement: This work was supported by the National Research Foundation of Korea (NRF) grant funded by the Korea government (MEST) (No. 314-2008-1-D00421). The authors wish to express their gratitude for the financial support that made this study possible.

References

Böhm, H.; Han, W.; Eckschlager, A. (2004): Multi-inclusion unit cell studies of reinforcement stresses and particle failure in discontinuously reinforced ductile matrix composites. *CMES: Computer Modeling in Engineering & Sciences* , vol. 5, pp. 5–20.

Cox, H. L. (1952): The elasticity and strength of paper and other fibrous materials. *British Journal of Applied Physics.*, vol. 122, no. 1, pp. 10-18.

Gao, Y. C.; Mai, Y. W.; Cotterell, B. (1988): Fracture of fiber-reinforced materials *J Appl Math Phys.*, vol. 39, pp. 550-558.

Kim, J. K.; Kim, J. S.; Ha, G. J.; Kim, Y. Y. (2007): Tensile and fiber dispersion performance of ECC (Engineered Cementitious Composites) produced with ground granulated blast furnace slag. *Cem Concr Res.*, vol. 37, no. 7, pp. 1096-1105.

Kanda, T.; Li, V. C. (2006): Practical design criteria for saturated pseudo strain-hardening behavior in ECC. *Journal of Advanced Concrete Technology*, vol. 4, no. 1, pp. 59-72.

Kanda, T.; Li, V. C. (1998): Interface property and apparent strength of a high strength hydrophilic fiber in cement matrix. *ASCE J Mater Civil Engng.*, vol. 10, no. 1, pp. 5-13.

Kanda, T.; Lin, Z.; Li, V. C. (2000): Tensile stress-strain modeling of pseudo strain-hardening cementitious composites. *ASCE J Mater Civil Engng.*, vol. 12, no. 2, pp. 147-156.

Leung, C. K. Y. (1996): Design criteria for pseudoductile fiber-reinforced composites. *ASCE J Engrg Mech.*, vol. 122, no. 1, pp. 10-14.

Lee, B. Y.; Kim, J. K.; Kim, J. S.; Kim, Y. Y. (2009): Quantitative Evaluation Technique of PVA (Polyvinyl Alcohol) Fiber Dispersion in Engineered Cementitious Composites. *Cem Concr Compos.*, vol. 31, no. 6, pp. 408-417.

Li, V. C. (1992): Post-crack scaling relations for fiber reinforced cementitious composites. *ASCE J Mater Civil Engng.*, vol. 4, no. 1, pp. 41-57.

Li, V. C.; Leung, C. K. Y. (1992): Steady-state and multiple cracking of short random fiber composites. *ASCE J Engrg Mech.*, vol. 118, no. 11, pp. 2246-2264.

Li, V. C.; Wu, C.; Wang, S.; Ogawa, A.; Saito, T. (2002): Interface tailoring for strain-hardening polyvinyl alcohol-engineered cementitious composite (PVA-

ECC). *ACI Mater J.*, vol. 99, no. 5, pp. 463-472.

Lin, Z.; Kanda, T.; Li, V. C. (1999): On interface property characterization and performance of fiber reinforced cementitious composites. *Concrete Science and Engineering (RILEM).*, vol. 1, pp. 173-184.

Marshall, D. B.; Cox, B. N. (1988): A J-integral method for calculating steady-state matrix cracking stressed in composites. *Mechanics of Materials.*, vol. 7,. no. 2, pp. 127-133.

Morton, J.; Groves, G. W. (1976): The effect of metal wires on the fracture of a brittle matrix composite. *J Mater Sci.*, vol. 11, pp. 617-622.

Pahr, D. H.; Böhm, H. J. (2008): Assessment of mixed uniform boundary conditions for predicting the mechanical behavior of elastic and inelastic discontinuously reinforced composites. *CMES: Computer Modeling in Engineering & Sciences*, vol. 34, pp. 117-136.

Pyo, S. H.; Lee, H. K. (2009): Micromechanical analysis of aligned and randomly oriented whisker-/ short fiber-reinforced composites. *CMES: Computer Modeling in Engineering & Sciences*, vol. 40, pp. 271-305.

Vincent, L. (1993): Morphological Grayscale Reconstruction in Image Analysis: Applications and Efficient Algorithms. *IEEE Trans Image Process*, vol. 2, no. 2, pp. 176-201.

Vincent, L.; Soille, P. (1991): Watesheds in digital spaces: An efficient algorithm based on immersion simulations. *IEEE Trans Patt Anal Machine Intell.*, vol. 13, no. 6, pp. 583-598.

Wu, C. (2001): Micromechanical tailoring of PVA-ECC for structural application. Ph. D. Thesis, University of Michigan,.

Xia, M.; Hamada, H. Maekawa, Z. (1995): Flexural Stiffness of Injection Molded Glass Fiber Reinforced Thermoplastics. *International Polymer Processing*, vol. 10, no. 1, pp. 74-81.

Yang, E. H.; Wang, S.; Yang, Y.; Li, V. C. (2008): Fiber-bridging constitutive law of engineered cementitious composites. *Journal of Advanced Concrete Technology.*, vol. 6, no. 1, pp. 181-193.